

Upconversion of Phonon Modes into Microwave Photons in a Lithium Niobate Bulk Acoustic Wave Resonator Coupled to a Microwave Cavity

S.Parashar*, W. M. Campbell, J.Bourhill, E.Ivanov, M.Goryachev, and M.E.Tobar*

Quantum Technologies and Dark Matter Labs, Department of Physics, University of Western Australia, 35 Stirling Highway, Crawley, WA 6009, Australia.^{a)}

The coupling between acoustic vibrations in a lithium niobate bulk acoustic wave resonator and microwave photons of a re-entrant microwave cavity was investigated at a temperature close to 4 K. Coupling was achieved by placing the acoustic resonator in the location of the re-entrant cavity electric field maxima, in a symmetric “split-post” configuration, with a large overlap between the microwave field and the acoustic mode, allowing acoustic modulations of the microwave frequency. We show that the acoustic modes in this setup retain large inherent quality factors of greater than 10^6 . A maximum optomechanical coupling rate was determined to be $g_0 = 0.014$ mHz, four orders of magnitude larger than previous results obtained using a quartz BAW at 4 K in a similar experimental setup, but using a single post-re-entrant cavity resonator.

Investigating the fundamental interaction between photonic and phononic systems is crucial for advancing various applications within the domain of quantum technology and quantum electrodynamics^{1,2}. This understanding has led to the emergence of numerous associated predicted phenomena. Resolved sideband cooling^{3,4}, parametric amplification^{5–7}, optomechanically induced transparency/absorption^{6,8}, and long-range entanglement^{9,10}, are just a few of these phenomena that have had important ramifications for testing fundamental quantum limits^{11–15}, dark matter detection^{16–18}, quantum communication, information processing and storage, along with generation and manipulation of quantum states^{19–21}. Importantly for these systems, highly coherent quantum state readouts and increased coupling rates are integral for parametric detection techniques. This is particularly relevant in the search for gravitons^{22,23} and in the development of parametric transducers for achieving low noise readouts at microwave frequencies^{3,24}.

Ground state preparation of truly macroscopic (gram-scale) mechanical resonators is a highly sought after experimental demonstration^{12,25,26}. For one, there still remain questions regarding the quantum-to-classical crossover point which will be revealed by such systems, but in addition, precision readout of such devices may offer insights into quantum gravity and high frequency gravitational wave detection.^{13,27–31}

Studies on these photon-phonon interactions employ various types of resonant photonic device architectures, such as superconducting circuits³², coplanar resonators³³, 3-D microwave cavity resonators³⁴, and whispering gallery resonators^{21,35,36}, combined with various types of mechanical architectures displaying high coupling rates, such as membrane-in-the-middle systems⁶, trapped ion particles³⁷, and acoustic-mechanical modes such as bulk acoustic wave (BAW) resonators^{6,25,26,35}. BAW resonators are low-loss me-

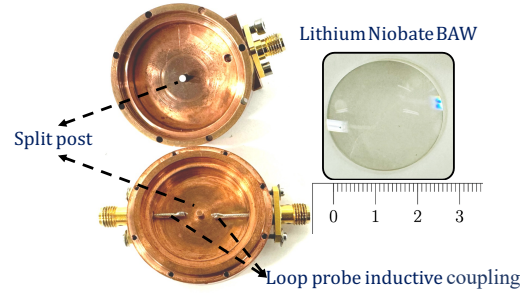


FIG. 1. The convex Lithium Niobate crystal BAW resonator, along with the two halves of the re-entrant split-post microwave cavity, fabricated from oxygen-free copper.

chanical resonators that exhibit long mechanical coherence times due to their specifically engineered convex surface, which helps trap the majority of phonons in the centre of the resonator²⁷.

In this work, a macroscopic centimetre size-scale lithium niobate (LiNbO_3) crystal with its axis cut in the z-direction was manufactured with a diameter of 30 mm, a centre thickness of 2 mm and a convex radius of curvature of 100 mm. The crystal exhibited coherent phonon modes trapped in the centre of the crystal with frequencies of order MHz. Fig.1 shows a photo of the LiNbO_3 crystal along with the two halves of a “split-post” microwave cavity resonator³⁸, which sandwiches the BAW in the post gap allowing maximum electric field to be applied to the region of maximum phonon trapping as shown in Fig. 2. This means the acoustic phonons will be parametrically upconverted to microwave frequencies. The motivation was drawn from similar experiments conducted with quartz BAW resonators^{26,39}. However, the cavity design differs from before as we have used a symmetric design in which the gap is located in the centre of a co-axial cavity. This particular design results in a more highly confined electric field distribution focused into the centre of the BAW, and we term this design the “split-post re-entrant cavity”. Moreover, the reason for the emerging popularity of LiNbO_3 over quartz is that it exhibits a stronger piezoelectric coefficient in addition

^{a)}Electronic mail: 23307714@student.uwa.edu.au; Electronic mail: michael.tobar@uwa.edu.au

to a low loss tangent. For example, LiNbO₃-BAW has demonstrated a high quality factor \times frequency product, of $\sim 10^{14}$ Hz at room temperature⁴⁰.

Much smaller LiNbO₃ nanostructures have been used previously in various optical applications, such as quantum sensors^{41,42} and optical transducers^{43–48}. Our study investigated LiNbO₃ microwave-BAW coupling rates, with the goal of creating strongly coupled coherent microwave readout of large macroscopic phonon modes for fundamental physics applications that require larger masses. Here upconversion opens up possibilities for harnessing effects such as parametric amplification, cooling, and squeezing, while also providing a method for reading out displacement in large non-piezoelectric crystals.

To model the photon-phonon interaction, the dynamics are characterized by the following Hamiltonian¹:

$$H = \hbar\omega_c a^\dagger a + \hbar\omega_m b^\dagger b + \hbar g_0 (a^\dagger a) (b^\dagger + b), \quad (1)$$

where $a(a^\dagger)$ and $b(b^\dagger)$ are the bosonic annihilation (creation) operators of the microwave and the acoustic resonance, at frequencies ω_c and ω_m , respectively, and g_0 is the optomechanical coupling rate.

The Hamiltonian in (1) describes the interaction between a microwave electric field between the two posts and the acoustic phonon mode of the BAW device, which results in radiation pressure acting on the acoustic modes. This radiation pressure displaces the oscillator (by displacement x) and leads to parametric modulation of the microwave cavity fields as shown in (2), where the second term on the RHS represents the linear coupling, which can be implemented as a displacement readout¹:

$$\omega_c(x) \approx \omega_c + x \frac{\delta\omega_c}{\delta x} + \dots \quad (2)$$

Furthermore, we can define the following quantities:

$$G = -\frac{\delta\omega_c}{\delta x} \quad \text{and} \quad g_0 = G x_{\text{zpf}}, \quad (3)$$

where G , also known as the frequency pull factor, is measured from the experimental data and helps evaluate g_0 , which is the photon-phonon coupling rate, also known as the single photon coupling rate. Additionally, $x_{\text{zpf}} = \sqrt{2\hbar/\omega_m M_{\text{eff},m}}$ is the zero-point fluctuation of the mechanical resonance, where \hbar is the reduced Planck's constant, and $M_{\text{eff},m}$ is the effective mode mass.

Fig. 2(a) illustrates the experimental setup for measurements conducted at 4 K. The experiment utilizes the split post microwave cavity, which functions as a frequency discriminator. This phase bridge detects frequency shifts of the cavity in response to mechanical modes by ensuring that the LO and RF signals are in quadrature, making the system insensitive to amplitude fluctuations. The power splitting ratio is set by a -6dB directional coupler. The signal generator is an analog synthesizer (Keysight E8663D), covering the frequency range of 100 kHz to 9 GHz. Thus the experiment measures the frequency modulation of the BAW resonator

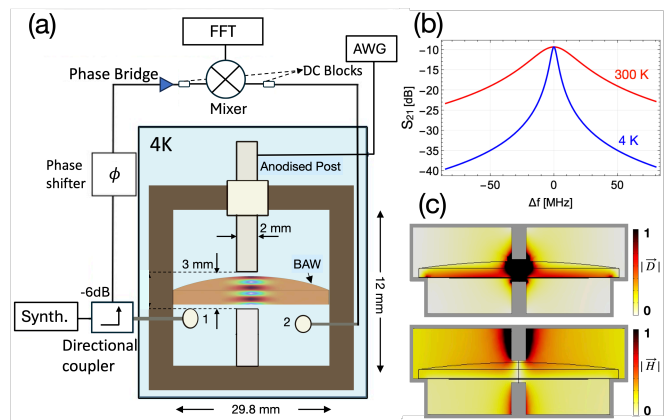


FIG. 2. a) Not to scale microwave-BAW cavity set-up with a frequency discriminator output. The synthesizer was tuned to the microwave cavity and measured at the mixer output with the FFT to detect the upconverted BAW frequency. b) Microwave transmission measurements (S_{21}) with a vector network analyser between ports 1 and 2, comparing 300 K with 4K, showing an increase microwave Q-factor. c) To scale electric flux density $|\vec{D}|$ and magnetic field intensity $|\vec{H}|$ density plots inside the split-post microwave cavity. The electric flux density is concentrated in the centre of the BAW in the vicinity of the MHz phonon modes, which are indicated in 2(a).

up-converted to microwave frequencies. The output of the mixer is observed on the FFT spectrum analyser.

The set-up in Fig. 2 also shows the two posts of the microwave cavity, one of which was anodised to provide two electrically isolated posts allowing them to function as electrodes to piezoelectrically excite the BAW mechanical modes with an arbitrary waveform generator (AWG). Since the applied voltage to the electrodes is known, we can estimate the piezoelectric-induced crystal displacement using known LiNbO₃ electrostatic material parameters, allowing us to determine the change in displacement dx . The measured change in microwave cavity frequency, $d\omega_c$, is then used to determine G .

It is known that for piezoelectric materials, the mechanical displacement x is proportional to the charge on the surface¹. In our set up, this charge is enhanced due to the split post geometry and is given by, $q = k_m x$, where, k_m is the effective piezoelectric coupling constant defined using the Butterworth-Van Dyke (BWD) model, which can be understood from the BAW-resonator lumped circuit element theory⁴⁹. For a mechanical mode, m , relations between piezoelectric constant and the corresponding LCR circuit elements of the BWD model are represented as²⁸:

$$M_{\text{eff},m} = k_m^2 L_m; \quad R_m = \frac{k_m^2}{C_m}; \quad \text{so that} \quad k_m^2 = \frac{\omega_m M_{\text{eff},m}}{Q_m R_m}. \quad (4)$$

Here, Q_m is the mode quality factor, R_m the motional resistance, and L_m and C_m the effective inductance and capacitance respectively. Similarly, the current from the

equivalent BAW circuit model may be presented in terms of mechanical resonance ω_m as:

$$I(\omega_m) = k_m \omega_m x. \quad (5)$$

Thus, the values of motional resistance could be measured at 4 K using an impedance analyser.

The operational cavity mode was the fundamental split-post-mode (Fig. 2c), with a frequency of 6.075 GHz at 4 K. The loaded quality factor, Q_L , improved significantly from 300 to 4 K, to $Q_L = 330$ to 2500 respectively, due to reduced resistive losses from the copper cavity walls as shown in Fig. 2b. The coupling coefficients were determined from reflection measurements from ports 1 and 2, and calculated to be $\beta_1 = 0.8$ and $\beta_2 = 0.136$. Thus the unloaded microwave Q -factor can thus be determined to be $Q_0 = Q_L(1 + \beta_1 + \beta_2) = 4250$. The increased Q -factor helped achieve better discriminator sensitivity for the phase bridge setup. The incident input power to the microwave cavity was 0.01 mW.

The change in the displacement of the mechanical mode is given by the simple relationship between the calculated displacement Δx and the change in the output voltage ΔV from the mixer, as follows:

$$\frac{\Delta V}{\Delta x} = \frac{dV}{d\omega_c} \frac{d\omega_c}{dx}, \quad (6)$$

where $dV/d\omega_c$ is the discriminator sensitivity (phase-bridge); the ratio at which frequency fluctuations are converted to synchronous voltage fluctuations in the read-out, while $G = -d\omega_c/dx$ is the frequency pull factor introduced previously and is evaluated from the voltage response output from the mixer corresponding to the displacement of mechanical resonance.

From (1), we can also calculate $\frac{d\omega_c}{dx}$ in terms of x_{zpf} :

$$\frac{d\omega_c}{dx} = \frac{g_0}{x_{zpf}}. \quad (7)$$

Driving an applied time varying MHz signal across the split-posts, piezoelectrically exciting the BAW, while simultaneously driving the microwave cavity at its resonant frequency, yields a mechanically induced frequency modulation of the microwave pump frequency, producing side bands on the microwave carrier. This is triggered by the induced displacement of the LiNbO₃ BAW when tuned to the acoustic modes. Due to the trigonal symmetry of lithium niobate, two-mode families exist. ‘A’ refers to longitudinal polarization, where bulk displacement occurs in the z-direction, while ‘B’ denotes a shear wave polarized mode with dominant displacement in the x-y plane. The first subscript refers to the fundamental polarization inside the BAW resonator, which has been studied in⁴⁰. More details of the different suffixes in the modes can be found in²⁷. In this work, we study the A_{3,0,0} and A_{5,0,0} longitudinal modes, and B_{5,0,0}, B_{7,0,0}, B_{9,0,0} shear modes.

Fig. 3 c) and d) shows the mixer output voltages for the longitudinal A_{5,0,0} mode and the shear B_{7,0,0} modes

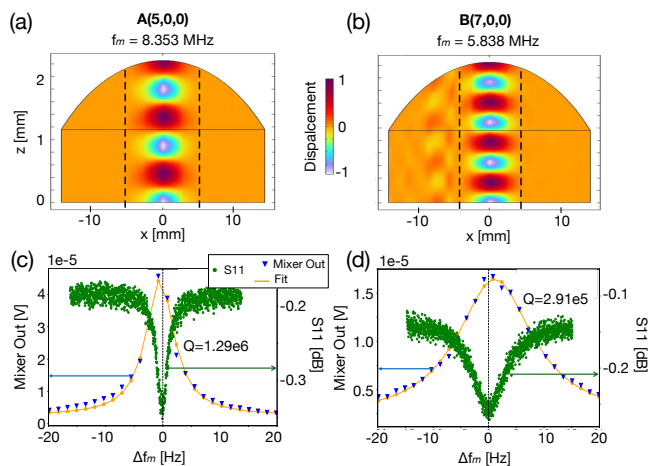


FIG. 3. FEM simulations of the displacement field of the a) 8.3 MHz longitudinal and b) 5.8 MHz shear modes, with dashed lines indicating the effective mode volumes. c) and d) show the corresponding mixer output voltage in blue and S_{11} reflection measurements in green using an impedance analyser across the split-post. Loaded Q -factors are determined by curve fits, as shown in orange.

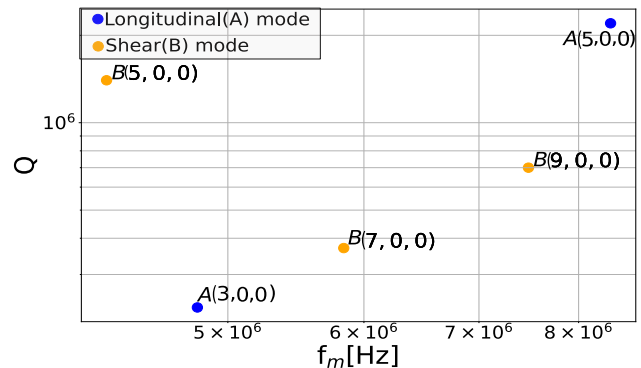


FIG. 4. Q values for the A_{3,0,0} and A_{5,0,0} longitudinal and B_{5,0,0}, B_{7,0,0}, and B_{9,0,0} shear modes, obtained from mixer trace output. The Q -factors demonstrate insignificant power dependence until the onset of duffing nonlinearity. The $Q \times f$ product of the best modes are of order 10^{14}

respectively. Normalised reflection coefficients S_{11} are measured by driving the BAW through the anodised post and measuring the reflected power on an impedance analyser, which is shown as the green trace. Fig. 3 illustrates that the mixer output voltage is indeed a result of the mechanical mode being driven. We can determine the linewidth of the mechanical modes from the mixer output voltage and obtain Q -factors. These values closely agree with the previously measured Q at 4 K using a parallel cathode plate⁴⁰. Fig. 4 shows measured mechanical Q -factors at 4 K for various A and B modes.

The effective mode mass for various A and B modes of the BAW vary slightly from each other, depending on the value of their lumped circuit parameters. These val-

ues were calculated using COMSOL finite element modelling, similar to the analysis for quartz, as detailed in the works of ^{12,26}, and related analytical effective mass calculations by ^{50,51}, with details given in Appendix A. Various determined parameters for each of the mechanical modes are presented in Table I, where co-operativity C_0 is defined as $C_0 = 4g_0^2/\Gamma_m\kappa_c$, Γ_m is the line width of the mechanical resonance and κ_c is the linewidth of the microwave cavity¹. As observed, different modes show different coupling rates due to different displacement polarisations and different overlaps between the re-entrant post-mode and the mechanical modes.

The displacement of the crystal structure is calculated from the electrical current arising from the applied piezoelectric voltage using equations (4) and (5). The frequency shift from the phase bridge measurement divided by the calculated piezoelectric induced displacement provides the frequency pull factor, as detailed by equations (6) and (7). By measuring Δf_c for different input voltages to the piezoelectric BAW (converted to displacements), coupling rates at 4 K for different modes were calculated from the gradients of df_c/dx . Fig. 5 shows coupling rates for A and B modes of LiNbO₃-BAW, compared to other mechanical resonators. The inset figure shows df_c/dx for the $A_{5,0,0}$ mode and is equal to 4.4×10^{13} Hz/m. The coupling rate g_0 is derived from this value by multiplying it with x_{zpf} .

The value of these coupling rates is benchmarked against similar experiments using a quartz BAW at 4 K with a single post-re-entrant resonator, as described in ^{26,39}. The coupling rates g_0 for LiNbO₃-BAW in the split-post re-entrant cavity are observed to be up to four orders of magnitude greater compared to quartz for the longitudinal mode at $A_{3,0,0}$, demonstrating higher coupling rates and making it a suitable candidate for further studies. Additionally, we compared our results with a Si₃N₄ membrane inside a re-entrant cavity, which achieved coupling rates of 25 mHz⁶. These findings motivate further investigation into the coupling of LiNbO₃-BAW with photonic systems.

The degree to which the electromagnetic and mechanical mode volumes overlap plays a key role in determining the optomechanical coupling. The improvement in coupling rates resulting from the use of a split-post versus a single-post cavity can be estimated by the ratios of a

$X_{n,m,p}$	f_m	$M_{\text{eff},m}$	g_0	C_0
B _{5,0,0}	4.20	3.53×10^{-4}	2.67×10^{-7}	2.40×10^{-20}
A _{3,0,0}	4.70	4.15×10^{-4}	1.44×10^{-5}	2.40×10^{-17}
B _{7,0,0}	5.80	3.14×10^{-4}	2.12×10^{-8}	2.96×10^{-23}
B _{9,0,0}	7.40	2.77×10^{-4}	4.79×10^{-8}	7.62×10^{-22}
A _{5,0,0}	8.30	3.52×10^{-4}	2.38×10^{-6}	1.96×10^{-18}

TABLE I. Comparison of the parameters for some BAW modes. Frequencies, f_m , in MHz⁴⁰; $M_{\text{eff},m}$ in gram, evaluated from finite element modelling; g_0 the coupling rate in Hz, and the single photon cooperativity, C_0 .

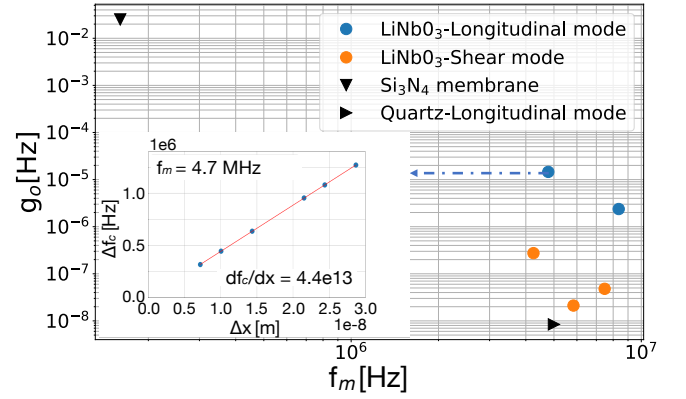


FIG. 5. Coupling rates for various A (blue) and B (orange) modes of the LiNbO₃-BAW at 4K, compared to other acoustic resonator coupling rates^{6,26,39}. The inset figure shows the change in microwave frequency Δf_c (Hz) corresponding to displacement Δx for $A_{5,0,0}$ mode, the slope of which multiplied by x_{zpf} gives g_0 .

so-called overlap factor. This factor can be determined from the percentage of electromagnetic mode that exists within the mechanical mode volume determined by the dashed lines in Fig. 3. The $A_{5,0,0}$ mechanical mode, for example, has all of its displacement field within a diameter of approximately 6.0 mm. Inside this volume, the electromagnetic field distribution for both the split- and single-post cavities is primarily determined by the E_z field, which makes up $> 99\%$ of the electrical energy, which is only 5% in the case of a single post. The amount of electrical field within the mechanical mode volume is 20 times larger for a split-post design compared to the single-post design, explaining one of the contributions to the observed coupling rate increase of these results compared to the results in quartz^{26,39}. The remaining contribution stems from the material properties.

In conclusion, we investigated the acoustic modes of a LiNbO₃-BAW resonator by directly exciting them with a radio frequency external voltage at mechanical resonance through piezoelectricity at 4 K. Coupling rates of order 0.014 mHz were obtained for the $A_{3,0,0}$ longitudinal mode, four orders of magnitude larger than previous results obtained using quartz. Thus, with further development, could be utilised as an alternate material in quantum sensing and communication, and testing of fundamental physics.

ACKNOWLEDGMENTS

This research was supported by the ARC Centre of Excellence for Engineered Quantum Systems (EQUS, No. CE170100009) along with support from the Defence Science and Technology Group (DSTG) as part of the EQUS Quantum Clock Flagship program. Additional support provided by the ARC Centre of Excellence for Dark Mat-

ter Particle Physics (CDM, No. CE200100008).

APPENDIX: SOME ACOUSTIC MODE PROPERTIES

A. Effective mass of the mechanical modes

Evaluation of mode mass was done using COMSOL, evaluating potential energy integral for 3D/2D model, for a given mode is given in terms of following equations.

$$dU = \frac{1}{2}\omega_m^2 |a_m(t)|^2 \rho(\mathbf{x}) dV. \quad (8)$$

The total potential energy of the mode is then given by, integral over the entire volume as represented by

$$U = \frac{1}{2} m_{\text{eff},m} \omega_m^2 |a_m(t)|^2. \quad (9)$$

Here material density is uniform and effective mass for a 3D model

$$m_{\text{eff},m} = \rho \int |\mathbf{r}_m(\mathbf{x})|^2 dV. \quad (10)$$

This process begins by evaluating the point displacement at the calculation point, as in the case of the odd mode, where the displacement at the point of maximum displacement is used to normalize the displacement function $\mathbf{r}_m(\mathbf{x})$. The integral of the normalized displacement over the entire geometry of the resonator is then multiplied by $\frac{\pi}{2} r \rho$ to obtain the effective mass (our model in COMSOL was a 2D axisymmetrical model). By investigating the potential energy U for any mode with a small volume element dV centred on \mathbf{x} the potential energy centred around the mass element $dm = \rho(\mathbf{x})dV$ and is defined as below, where $m_{\text{eff},m}$ is defined as effective modal mass for a given mode m .

B. Power dependence of the mechanical mode

Fig. 6 shows the density plot for A(5,0,0) mode where the input voltage to the cavity is varied in the range of 0.1 V-3.0 V, and the output of the mixer is plotted for different input power. As the power is increased the amplitude of the sideband increases, however there is no significant change in line-width, which indicated no variation in Q-factor.

REFERENCES

- ¹M. Aspelmeyer, T. J. Kippenberg, and F. Marquardt, “Cavity optomechanics,” *Reviews of Modern Physics* **86**, 1391 (2014).
- ²A. Blais, A. L. Grimsmo, S. M. Girvin, and A. Wallraff, “Circuit quantum electrodynamics,” *Reviews of Modern Physics* **93**, 025005 (2021).

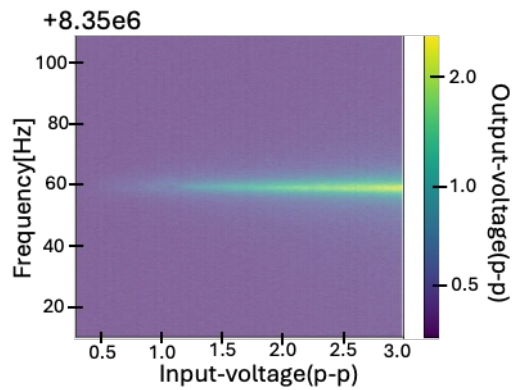


FIG. 6. Mixer output voltage for varying input power of the A(5,0,0) mode.

- ³B. Cuthbertson, M. Tobar, E. Ivanov, and D. Blair, “Parametric back-action effects in a high-Q cryogenic sapphire transducer,” *Review of Scientific Instruments* **67**, 2435–2442 (1996).
- ⁴J. D. Teufel, T. Donner, D. Li, J. W. Harlow, M. S. Allman, K. Cicak, A. J. Sirois, J. D. Whittaker, K. W. Lehnert, and R. W. Simmonds, “Sideband cooling of micromechanical motion to the quantum ground state,” *Nature* **475**, 359–363 (2011).
- ⁵D. J. Wilson, V. Sudhir, N. Piro, R. Schilling, A. Ghadimi, and T. J. Kippenberg, “Measurement-based control of a mechanical oscillator at its thermal decoherence rate,” *Nature* **524**, 325–329 (2015).
- ⁶S. Kumar, M. Kenworthy, H. Ginn, and X. Rojas, “Optomechanically induced transparency/absorption in a 3D microwave cavity architecture at ambient temperature,” *AIP Advances* **14**, 035107 (2024).
- ⁷H. Xiong and Y. Wu, “Fundamentals and applications of optomechanically induced transparency,” *Applied physics reviews* **5** (2018).
- ⁸G. S. Agarwal and S. Huang, “Electromagnetically induced transparency in mechanical effects of light,” *Physical Review A—Atomic, Molecular, and Optical Physics* **81**, 041803 (2010).
- ⁹X. Yao, M. H. de Jong, J. Li, and S. Gröblacher, “Long-range optomechanical interactions in sin membrane arrays,” *arXiv preprint arXiv:2408.03066* (2024).
- ¹⁰T. Palomaki, J. Teufel, R. Simmonds, and K. W. Lehnert, “Entangling mechanical motion with microwave fields,” *Science* **342**, 710–713 (2013).
- ¹¹B. Schirnski, Y. Yang, U. Von Lüpke, M. Bild, Y. Chu, K. Hornberger, S. Nimmrichter, and M. Fadel, “Macroscopic quantum test with bulk acoustic wave resonators,” *Physical Review Letters* **130**, 133604 (2023).
- ¹²P. Bushev, J. Bourhill, M. Goryachev, N. Kukharchyk, E. Ivanov, S. Galliou, M. Tobar, and S. Danilishin, “Testing the generalized uncertainty principle with macroscopic mechanical oscillators and pendulums,” *Physical Review D* **100**, 066020 (2019).
- ¹³W. M. Campbell, M. E. Tobar, M. Goryachev, and S. Galliou, “Improved constraints on minimum length models with a macroscopic low loss phonon cavity,” *Physical Review D* **108**, 102006 (2023).
- ¹⁴A. Lo, P. Haslinger, E. Mizrachi, L. Anderegg, H. Müller, M. Hohensee, M. Goryachev, and M. E. Tobar, “Acoustic tests of Lorentz symmetry using quartz oscillators,” *Physical Review X* **6**, 011018 (2016).
- ¹⁵M. Goryachev, Z. Kuang, E. N. Ivanov, P. Haslinger, H. Müller, and M. E. Tobar, “Next generation of phonon tests of Lorentz invariance using quartz baw resonators,” *IEEE Transactions on Ultrasonics, Ferroelectrics, and Frequency Control* **65**, 991–1000 (2018).

- ¹⁶A. Arvanitaki, S. Dimopoulos, and K. Van Tilburg, “Sound of dark matter: searching for light scalars with resonant-mass detectors,” *Physical review letters* **116**, 031102 (2016).
- ¹⁷D. Carney, A. Hook, Z. Liu, J. M. Taylor, and Y. Zhao, “Ultra-light dark matter detection with mechanical quantum sensors,” *New Journal of Physics* **23**, 023041 (2021).
- ¹⁸W. M. Campbell, B. T. McAllister, M. Goryachev, E. N. Ivanov, and M. E. Tobar, “Searching for scalar dark matter via coupling to fundamental constants with photonic, atomic, and mechanical oscillators,” *Physical Review Letters* **126**, 071301 (2021).
- ¹⁹V. J. Gokhale, B. P. Downey, D. S. Katzer, N. Nepal, A. C. Lang, R. M. Stroud, and D. J. Meyer, “Epitaxial bulk acoustic wave resonators as highly coherent multi-phonon sources for quantum acoustodynamics,” *Nature communications* **11**, 2314 (2020).
- ²⁰Y. Chu, P. Kharel, W. H. Renninger, L. D. Burkhardt, L. Frunzio, P. T. Rakich, and R. J. Schoelkopf, “Quantum acoustics with superconducting qubits,” *Science* **358**, 199–202 (2017).
- ²¹P. Salzenstein, A. Kuna, L. Sojdr, and J. Chauvin, “Significant step in ultra high stability quartz crystal oscillators,” *Electron. Lett* **46**, 1433–1434 (2010).
- ²²G. Tobar, S. K. Manikandan, T. Beitel, and I. Pikovski, “Detecting single gravitons with quantum sensing,” *Nature Communications* **15**, 7229 (2024).
- ²³G. Tobar, I. Pikovski, and M. E. Tobar, “Detecting kHz gravitons from a neutron star merger with a multi-mode resonant bar,” arXiv preprint arXiv:2406.16898 (2024).
- ²⁴C. Locke, M. Tobar, E. Ivanov, and D. Blair, “Parametric interaction of the electric and acoustic fields in a sapphire monocrystal transducer with a microwave readout,” *J. Appl. Phys.* **84**, 6523–6527 (1998).
- ²⁵J. Bourhill, E. Ivanov, and M. Tobar, “Precision measurement of a low-loss cylindrical dumbbell-shaped sapphire mechanical oscillator using radiation pressure,” *Physical Review A* **92**, 023817 (2015).
- ²⁶J. Bourhill, N. d. C. Carvalho, M. Goryachev, S. Galliou, and M. E. Tobar, “Generation of coherent phonons via a cavity enhanced photonic lambda scheme,” *Applied Physics Letters* **117** (2020).
- ²⁷M. Goryachev and M. E. Tobar, “Gravitational wave detection with high frequency phonon trapping acoustic cavities,” *Physical Review D* **90**, 102005 (2014).
- ²⁸W. M. Campbell, M. Goryachev, and M. E. Tobar, “The multi-mode acoustic gravitational wave experiment: Mage,” *Scientific Reports* **13**, 10638 (2023).
- ²⁹M. Goryachev, W. M. Campbell, I. S. Heng, S. Galliou, E. N. Ivanov, and M. E. Tobar, “Rare events detected with a bulk acoustic wave high frequency gravitational wave antenna,” *Physical Review Letters* **127**, 071102 (2021).
- ³⁰S. Singh, L. De Lorenzo, I. Pikovski, and K. Schwab, “Detecting continuous gravitational waves with superfluid ^4He ,” *New Journal of Physics* **19**, 073023 (2017).
- ³¹N. Aggarwal, O. D. Aguiar, A. Bauswein, G. Cella, S. Clesse, A. M. Cruise, V. Domcke, D. G. Figueroa, A. Geraci, M. Goryachev, *et al.*, “Challenges and opportunities of gravitational-wave searches at mhz to ghz frequencies,” *Living reviews in relativity* **24**, 1–74 (2021).
- ³²A. Blais, S. M. Girvin, and W. D. Oliver, “Quantum information processing and quantum optics with circuit quantum electrodynamics,” *Nature Physics* **16**, 247–256 (2020).
- ³³R. Manenti, A. F. Kockum, A. Patterson, T. Behrle, J. Rahamim, G. Tancredi, F. Nori, and P. J. Leek, “Circuit quantum acoustodynamics with surface acoustic waves,” *Nature communications* **8**, 975 (2017).
- ³⁴J. Kitzman, J. Lane, C. Undershute, M. Drimmer, A. Schleusner, N. Beysengulov, C. Mikolas, and J. Pollanen, “Free-space coupling and characterization of transverse bulk phonon modes in lithium niobate in a quantum acoustic device,” *Appl. Phys. Lett.* **123**, 224001 (2023).
- ³⁵A. Schliesser and T. J. Kippenberg, “Cavity optomechanics with whispering-gallery mode optical micro-resonators,” in *Advances In Atomic, Molecular, and Optical Physics*, Vol. 58 (Elsevier, 2010) pp. 207–323.
- ³⁶C. Locke and M. Tobar, “Measurement of the strain-induced coefficient of permittivity of sapphire using whispering gallery modes excited in a high-q acoustic sapphire oscillator,” *Measurement Science and Technology* **15**, 2145 (2004).
- ³⁷S. Kotler, R. W. Simmonds, D. Leibfried, and D. J. Wineland, “Hybrid quantum systems with trapped charged particles,” *Physical Review A* **95**, 022327 (2017).
- ³⁸J.-M. Le Floch, Y. Fan, M. Aubourg, D. Cros, N. Carvalho, Q. Shan, J. Bourhill, E. Ivanov, G. Humbert, V. Mdrangeas, *et al.*, “Rigorous analysis of highly tunable cylindrical transverse magnetic mode re-entrant cavities,” *Rev. Sci. Instrum.* **84**, 125114 (2013).
- ³⁹N. Carvalho, J. Bourhill, M. Goryachev, S. Galliou, and M. Tobar, “Piezo-optomechanical coupling of a 3D microwave resonator to a bulk acoustic wave crystalline resonator,” *Appl. Phys. Lett.* **115**, 211102 (2019).
- ⁴⁰W. M. Campbell, S. Parashar, M. E. Tobar, and M. Goryachev, “Low temperature properties of low-loss macroscopic lithium niobate bulk acoustic wave resonators,” preprint arXiv:2407.17693 (2024).
- ⁴¹I. Marinkovic, M. Drimmer, B. Hensen, and S. Groblacher, “Hybrid integration of silicon photonic devices on lithium niobate for optomechanical wavelength conversion,” *Nano letters* **21**, 529–535 (2021).
- ⁴²A. Y. Cleland, E. A. Wollack, and A. H. Safavi-Naeini, “Studying phonon coherence with a quantum sensor,” *Nature Communications* **15**, 4979 (2024).
- ⁴³P. Arrangoiz-Arriola, E. A. Wollack, M. Pechal, J. D. Witmer, J. T. Hill, and A. H. Safavi-Naeini, “Coupling a superconducting quantum circuit to a phononic crystal defect cavity,” *Physical Review X* **8**, 031007 (2018).
- ⁴⁴K. J. Satzinger, Y. Zhong, H.-S. Chang, G. A. Peairs, A. Bienfait, M.-H. Chou, A. Cleland, C. R. Conner, É. Dumur, J. Grebel, *et al.*, “Quantum control of surface acoustic-wave phonons,” *Nature* **563**, 661–665 (2018).
- ⁴⁵L. Shao, M. Yu, S. Maity, N. Sinclair, L. Zheng, C. Chia, A. Shams-Ansari, C. Wang, M. Zhang, K. Lai, and M. Lončar, “Microwave-to-optical conversion using lithium niobate thin-film acoustic resonators,” *Optica* **6**, 1498–1505 (2019).
- ⁴⁶M. Mirhosseini, A. Sipahigil, M. Kalaei, and O. Painter, “Superconducting qubit to optical photon transduction,” *Nature* **588**, 599–603 (2020).
- ⁴⁷W. Jiang, C. J. Sarabalis, Y. D. Dahmani, R. N. Patel, F. M. Mayor, T. P. McKenna, R. Van Laer, and A. H. Safavi-Naeini, “Efficient bidirectional piezo-optomechanical transduction between microwave and optical frequency,” *Nature Communications* **11**, 1166 (2020).
- ⁴⁸E. A. Wollack, A. Y. Cleland, P. Arrangoiz-Arriola, T. P. McKenna, R. G. Gruenke, R. N. Patel, W. Jiang, C. J. Sarabalis, and A. H. Safavi-Naeini, “Loss channels affecting lithium niobate phononic crystal resonators at cryogenic temperature,” *Appl. Phys. Lett.* **118**, 123501 (2021).
- ⁴⁹S. Bible, “Crystal oscillator basics and crystal selection for rf-PICTM and PICmicro® devices,” *Microchip Technology Inc* (2002).
- ⁵⁰D. Stevens and H. Tiersten, “An analysis of doubly rotated quartz resonators utilizing essentially thickness modes with transverse variation,” *The Journal of the Acoustical Society of America* **79**, 1811–1826 (1986).
- ⁵¹J. Shi, C. Fan, M. Zhao, and J. Yang, “Variational formulation of the Stevens-Tiersten equation and application in the analysis of rectangular trapped-energy quartz resonators,” *The Journal of the Acoustical Society of America* **135**, 175–181 (2014).